Journal of Alloys and Compounds 866 (2021) 158778

Contents lists available at ScienceDirect

Journal of Alloys and Compounds

journal homepage: www.elsevier.com/locate/jalcom

Facile synthesis of triple Ni-Mo-W alloys and their catalytic properties in chemical vapor deposition of chlorinated hydrocarbons

Yury V. Shubin[a,b], Yury I. Bauman[c], Pavel E. Plyusnin[a], Ilya V. Mishakov[b,c], Maria S. Tarasenko[a], Maxim S. Mel'gunov[b,c], Vladimir O. Stoyanovskii[c], Aleksey A. Vedyagin[c,*]

[a] Nikolaev Institute of Inorganic Chemistry SB RAS, Novosibirsk, Russian Federation
[b] National Research Novosibirsk State University, Novosibirsk, Russian Federation
[c] Boreskov Institute of Catalysis SB RAS, Novosibirsk, Russian Federation

ARTICLE INFO

Article history:
Received 11 November 2020
Received in revised form 26 December 2020
Accepted 15 January 2021
Available online 1 February 2021

Keywords:
Nickel alloys
X-ray diffraction analysis
1,2-Dichloroethane
CCVD
Carbon nanofibers

ABSTRACT

The utilization of chlorine-containing organic wastes remains an actual problem. In the present research, sponge-like porous Ni-Mo-W alloys were prepared and used as catalysts for the catalytic chemical vapor deposition of 1,2-dichloroethane. The synthesis of the alloys was performed via a facile approach of high-temperature reductive thermolysis of the preliminarily prepared multicomponent precursors. The formation of alloys of exact composition was proven by precise X-ray diffraction analysis. The catalytic activity of the alloys in the decomposition of 1,2-dichloroethane was studied in a flow-through reactor at 600 °C for 2 h. The simultaneous presence of Mo and W in the composition of the Ni-based alloys was shown to have a synergetic effect on the process efficiency. The diameter of these fibers was found to be comparable with the size of metal particles formed as a result of initial alloys self-disintegration under the action of the aggressive reaction medium.

1. Introduction

Chlorinated organic compounds represent a class of hazardous substances strongly affecting living organisms due to their toxic and carcinogenic properties [1–5]. A lack and complicity of the processing technologies facilitate their contamination in soil, groundwater, and industrial wastewater and exhaust gases [6–10]. Therefore, the development of an efficient approach to the degradation of organochlorines is of great importance. Among the existing removal and neutralization techniques, catalytic methods should be specially mentioned [11–17].

In general, all the catalytic processing approaches can be divided into three groups: (i) oxidative degradation [18–20]; (ii) hydrodechlorination [21–25]; and (iii) hydrogen-assisted decomposition on carbon and HCl [26–30]. The group (i) quite often can lead to the formation of secondary pollutants, which, due to the simultaneous presence of chlorine and oxygen in a molecule, exhibit even higher toxicity. The second group (ii) allows recovering of olefins and their cycling into the technological process, but this approach is hardly applicable for the processing of complex organochlorine mixtures. The last group (iii) is more versatile and can be applied for the conversion of a wide range of chlorinated compounds, including their complex mixtures. This approach is based on the catalytic chemical vapor deposition (CCVD) process taking place over the iron subgroup metals in accordance with the so-called carbide cycle mechanism [27,28,31–33].

The Ni-containing catalytic systems, including bulk nickel alloys, were recently shown to be more active and prospective for CCVD of 1,2-dichloroethane, taken as a model organochlorine substance [33]. Pure nickel catalyzes the process but undergoes a rapid deactivation after few hours of exploitation due to the coking of the active sites. Alloying of Ni with other metals was found to enhance the stability and efficiency of the catalyst significantly. For instance, noticeable positive effects were observed for the nickel catalysts alloyed with chromium [28], palladium [34], and platinum [35,36]. The addition of molybdenum instead of the mentioned metals gives an even more exciting effect [37]. As we have reported recently [37–39], the content of molybdenum in the Ni-Mo catalysts affects their activity and efficiency in the CCVD of 1,2-dichloroethane. The comparison analysis of Mo-containing catalysts with other bimetallic systems (Ni-Co, Ni-Cr, Ni-Cu, Ni-Fe, and Ni-Pd) revealed that Mo is the most efficient additive, which allows Ni reaching the superior activity [40]. These catalysts provide a record high yield of carbon (up to 15 g_{CNF}/g_{cat}·h), and the obtained carbon nanofibers possess a

* Corresponding author.
E-mail address: vedyagin@catalysis.ru (A.A. Vedyagin).

https://doi.org/10.1016/j.jallcom.2021.158778
0925-8388/

developed surface area of 200–400 m^2/g and a unique segmented structure called a feathery-like structure. It was found that the catalytic activity depends non-linearly on the molybdenum concentration, and the maximum corresponds to 7–9 wt%. An introduction of the third component in the composition of Ni-Mo alloy is expected to open new possibilities for the creation of an even more active catalyst. In order to choose the third component, an analysis of the phase diagrams of the binary and triple systems was performed. It is important to note that the metal-carbon phase diagrams should be taken into account as well. The process of the CNF formation over iron subgroup metals (Fe, Co, Ni) proceeds in accordance with the so-called carbide cycle mechanism when the formation of intermediate non-stoichiometric carbides on the metal surface is considered [31]. Therefore, the ability of the doping metal to form the interstitial solid solution with carbon seems to be one of the necessary conditions to obtain the active catalyst. The Ni-Mo-W system meets these requirements.

In the present research, specially prepared sponge-like porous nanoscale Ni-W-Mo alloys were used as catalysts for the CCVD process of 1,2-dichloroethane (DCE). Such alloys attract a growing interest of researchers since they provide a developed porous structure along with considerable resistance to sintering at elevated temperatures that make it possible to use them under high-temperature reaction conditions [41]. The prepared Ni-W-Mo samples were studied by scanning electron microscopy and X-ray diffraction analysis, and their catalytic activity was examined in the hydrogen-assisted catalytic decomposition of DCE, resulting in the formation of carbon nanofibers (CNF). The effect of W and Mo addition on the catalytic activity of the alloys has been elucidated. The resulting CNF materials were investigated by low-temperature nitrogen adsorption, Raman spectroscopy, and transmission electron microscopy.

2. Experimental

2.1. Synthesis of the alloys

The starting reagent used for the preparation of alloys were $NiCl_2{\cdot}6H_2O$ (Reachem, Russia), H_2WO_4 (Vekton, Russia), and $(NH_4)_6Mo_7O_{24}{\cdot}4H_2O$ (Reachem, Russia). $[Ni(NH_3)_6]Cl_2$ was synthesized in accordance with the procedure described elsewhere [42]. Acetone was used as a precipitating agent. All the reagents were of chemical purity grade and were used without any preliminary purification.

In the case of Ni(92)Mo(4)W(4) preparation, H_2WO_4 (0.054 g) and $(NH_4)_6Mo_7O_{24}{\cdot}4H_2O$ (0.073 g) were dissolved in a concentrated ammonia solution (50 ml) at heating. Thus obtained solution was evaporated to a volume of 30 ml. Then, 3.633 g of $[Ni(NH_3)_6]Cl_2$ was added to the obtained solution at continuous stirring until complete dissolution. Thus obtained joint solution was added at intensive stirring to the 15-fold volume of acetone (450 ml) cooled to 0 °C. The sediment was filtered, dried at room temperature for 5 h, and calcined at 800 °C for 1 h in a hydrogen atmosphere. Similar procedures were applied for the preparation of all other precursors. The chemical composition and purity of the Ni-Mo-W alloys were controlled by an inductively coupled plasma atomic emission spectroscopy (ICP-AES) method. The samples were labeled as Ni(x)Mo(y)W(z), where x, y, and z is content (wt%) of Ni, Mo, and W, correspondingly.

The monometallic sample Ni(100) and bimetallic reference samples Ni-W(x) and Ni-Mo(x), where x is content (wt%) of W or Mo, were obtained by similar procedures.

2.2. Characterization techniques

The elemental analysis of metal content in the alloy samples was performed by an atomic absorption method using a Thermo Scientific iCAP-6500 spectrometer. The sample was dissolved in an aqua regis at heating and then evaporated with hydrochloric acid up to the complete removal of nitric acid. The relative standard deviation of the Mo and W determination was 0.1.

Simultaneous thermal analysis (STA) involved concurrent thermogravimetry (TG), differential thermal analysis (DTA), and mass spectral (MS) analysis of the evolved gas (EGA). The STA measurements were performed in an apparatus consisting of an STA 449 F1 Jupiter thermal analyzer and a 403D Aëolos quadrupole mass spectrometer (NETZSCH, Germany). The spectrometer was connected online to a thermal analyzer (STA) instrument by a quartz capillary heated to 280 °C. The mass spectrometer operated with an electron impact ionizer with an energy of 70 eV. The ion currents of the selected mass/charge (m/z) numbers were monitored in a multiple ions detection mode with a collection time of 0.1 s for each channel. The measurements were made using Al_2O_3 crucible in a hydrogen-helium mixture (10 vol% H_2) in a temperature range of 30–600 °C, a flow rate of 30 ml/min, and a heating rate of 1–10 °C/min.

The powder X-ray diffraction (XRD) analysis of the samples was performed at room temperature on a Shimadzu XRD-7000 diffractometer (CuKα radiation, nickel filter in reflected beam, scintillation detector with amplitude discrimination). The data were collected step-by-step in 2θ ranges of 20–100° with a step of 0.1° (for the phase identification) and 140–148° with a step of 0.05° (for the precise determination of lattice parameter). The lattice parameters of the alloys were refined by an angular position of the (331) reflection using the PowderCell 2.4 software Kraus [43].

Porous structure was characterized by means of the adsorption porosimetry using N_2 as adsorbate at 77.4 K on an ASAP-2400 (Micromeritics, USA) instrument. Before the adsorption experiments, the samples were stepwise degassed under fore-vacuum at 90 °C for 4 h and at 350 °C overnight.

The scanning electron microscopy (SEM) study of the initial alloys and produced carbon nanomaterials was carried out using a JSM-6460 scanning electron microscope (JEOL, Japan). The magnification factors were in a range of 8–300,000. The elemental mapping of the samples was performed by means of energy-dispersive X-ray (EDX) analysis.

The transmission electron microscopy (TEM) images were obtained using a Hitachi HT7700 microscope equipped with an EDX detector Bruker X-flash 6 T/60. The accelerating voltage was 100 kV.

Raman spectra of the samples were collected on a Horiba Jobin Yvon LabRAM HR UV–VIS–NIR Evolution Raman spectrometer equipped with an Olympus BX41 microscope and 514.5 nm line of Ar-ion laser. The power of light focused in a spot with a diameter of ~2 μm was less than 0.8 mW to avoid the thermal decomposition of the sample.

2.3. Catalytic performance measurements

The catalytic chemical vapor deposition (CCVD) of 1,2-dichloroethane (DCE) over the prepared triple Ni-W-Mo alloys was performed in a flow-bed quartz reactor equipped with MacBain balances. Therefore, the mass changes during the carbon product deposition were controlled in a *real-time* regime. The specimen of the alloy (2.0 ± 0.03 mg) was loaded in a quartz basket and heated in argon flow up to 600 °C. The next stage was reductive pretreatment in a hydrogen stream for 15 min, which allowed us to eliminate

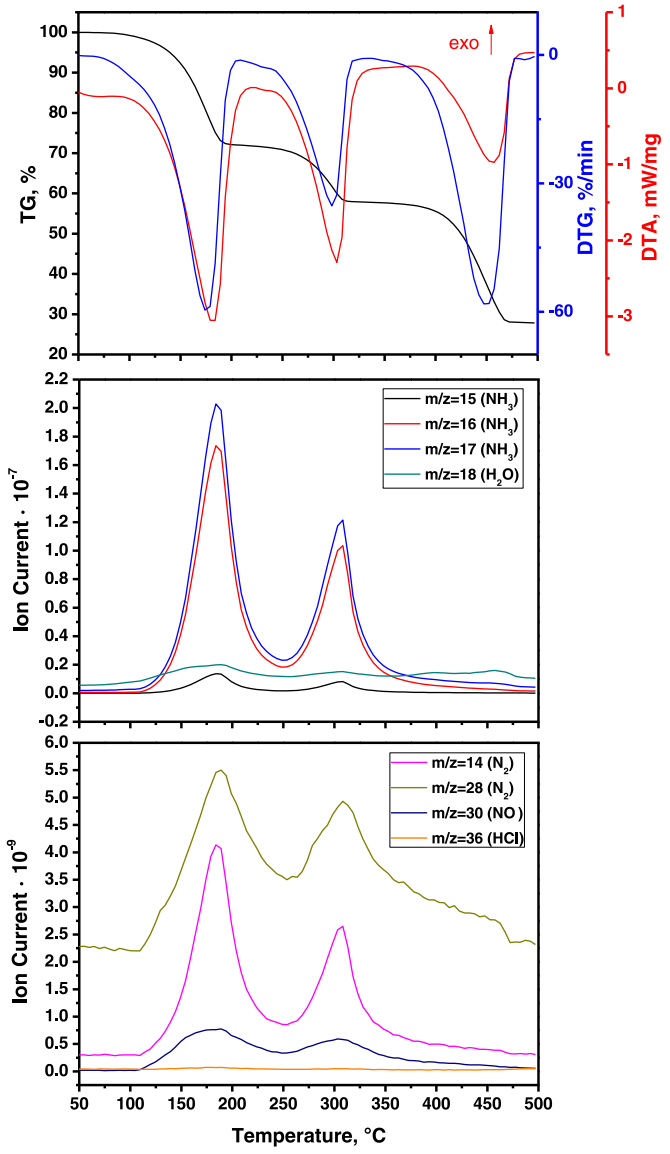

Fig. 1. Data of the thermal and mass spectral analyses for the decomposition of the Ni(92)Mo(4)W(4) catalyst's precursor in a hydrogen-helium mixture.

the residual oxygen from the sample's surface. The reduced sample was brought to contact with a reaction mixture containing 7 vol% DCE, 37 vol% hydrogen, and 56 vol% argon. The reaction gas feed rate was 15 l/h. The gaseous mixture from the reactor outlet was passed through the alkali trap (concentrated NaOH solution) to capture the HCl vapors resulted from the DCE decomposition. After 2 h of experiment, the reactor was cooled down in an argon flow to room temperature. The deposited carbon product was weighed, and the productivity of the alloy was calculated as grams of CNM produced per 1 g of the alloy sample.

3. Results and discussions

The synthesis of the sponge-like porous Ni-W-Mo alloys was performed via a facile approach of high-temperature reductive thermolysis of the preliminarily prepared precursors. The simplicity of the multicomponent precursor synthesis is in the precipitation of a micro-heterogeneous mixture of the initial components from an aqueous solution by mixing with an organic solvent. Thus, a high-concentrated joint solution of $[Ni(NH_3)_6]Cl_2$, $(NH_4)_6Mo_7O_{24}$, and $(NH_4)_2WO_4$ taken in the appropriate ratio was poured at intensive stirring into a large volume of acetone cooled to 0 °C. Due to the low solubility of the components in acetone, the formation of an oversaturated solution occurs, leading to the instantaneous precipitation of the multicomponent precursor. The further procedures of drying and calcination in a reductive medium result in the appearance of the metallic alloys of the desired composition. Thermal decomposition of the catalyst's precursors with various metal ratios proceeds through similar stages. The results of the thermal and mass spectral analyses are shown in Fig. 1. As seen, the precursor decomposes via three stages accompanied by endothermic effects. The first and second stages appear in temperature ranges of 80–220 °C and 250–330 °C, correspondingly. The main gaseous product here is ammonia registered as ion currents with the *m/z* values of 15, 16, and 17. Besides it, small amounts of nitrogen and NO are also observed. All these correspond to the decomposition of the initial precursor with the formation of a roentgen-amorphous mixture of nickel chloride and oxides of molybdenum and tungsten. The third stage appeared in a range of 350–480 °C results in a complete reduction of the intermediate product. Here, the main gaseous product is water.

The SEM images of thus obtained samples are shown in Fig. 2. According to the electron microscopy data, the alloys possess a micro-domain structure, consisting of the connected fragments. The average size of these fragments is affected by the ratio of the alloying metals. For instance, the binary Ni(92)Mo(8) and Ni(92)W(8) alloys have a very close structure with an average domain size of about 2 μm (Fig. 2a, f). The addition of W to the Ni-Mo alloy decreases the domain size. Thus, for the Ni(92)Mo(7)W(1) system (Fig. 2b), this size is estimated to be of ~1.5 μm. Further increase in the W content diminishes the size to the values of ~1 and ~0.5 μm for the samples Ni(92)Mo(4)W(4) and Ni(92)Mo(1)W(7), correspondingly (Fig. 2c–e). In principle, a decrease in the domain size and the developed porous structure should enhance the active sites' accessibility for the reagents.

In the next stages of the study, Mo:W ratio was 1:1, while the Ni:[Mo-W] ratio was varied. The results of the precise XRD analysis of the alloy samples are presented in Fig. 3 and Table 1. The XRD patterns of the alloys contain a set of reflexes attributed to a single fcc phase (sp.gr. Fm3m). A shift of reflexes with respect to their position for pure nickel is well seen in a far-angle area (Fig. 3b). This indicates the formation of solid solutions based on nickel lattice. The atomic radii of Mo and W are larger than the atomic radius of Ni. Therefore, the entry of these metals into Ni lattice regularly leads to an increase in the lattice parameter of the alloy. The analysis of the reflex position in the far-angle area testifies to this fact. As seen, an increase in the content of Mo and W shifts the reflex position to the small-angle area, thus giving evidence for an increase in the lattice parameter. The lattice parameters for the Ni-Mo, Ni-W, and Ni-Mo-W alloys calculated from the position of (311) reflex depending on the content of the alloying metal are given in Table 1.

The obtained dependencies are plotted in Fig. 4. As follows from the plots, the values of the lattice parameters for ternary Ni-Mo-W alloys are linearly fitted and located on equal distances from the corresponding fitting plots for the Ni-Mo and Ni-W alloys. Thereby, it can be concluded that the composition of the synthesized ternary alloys corresponds to the calculated composition predefined during the preparation procedures.

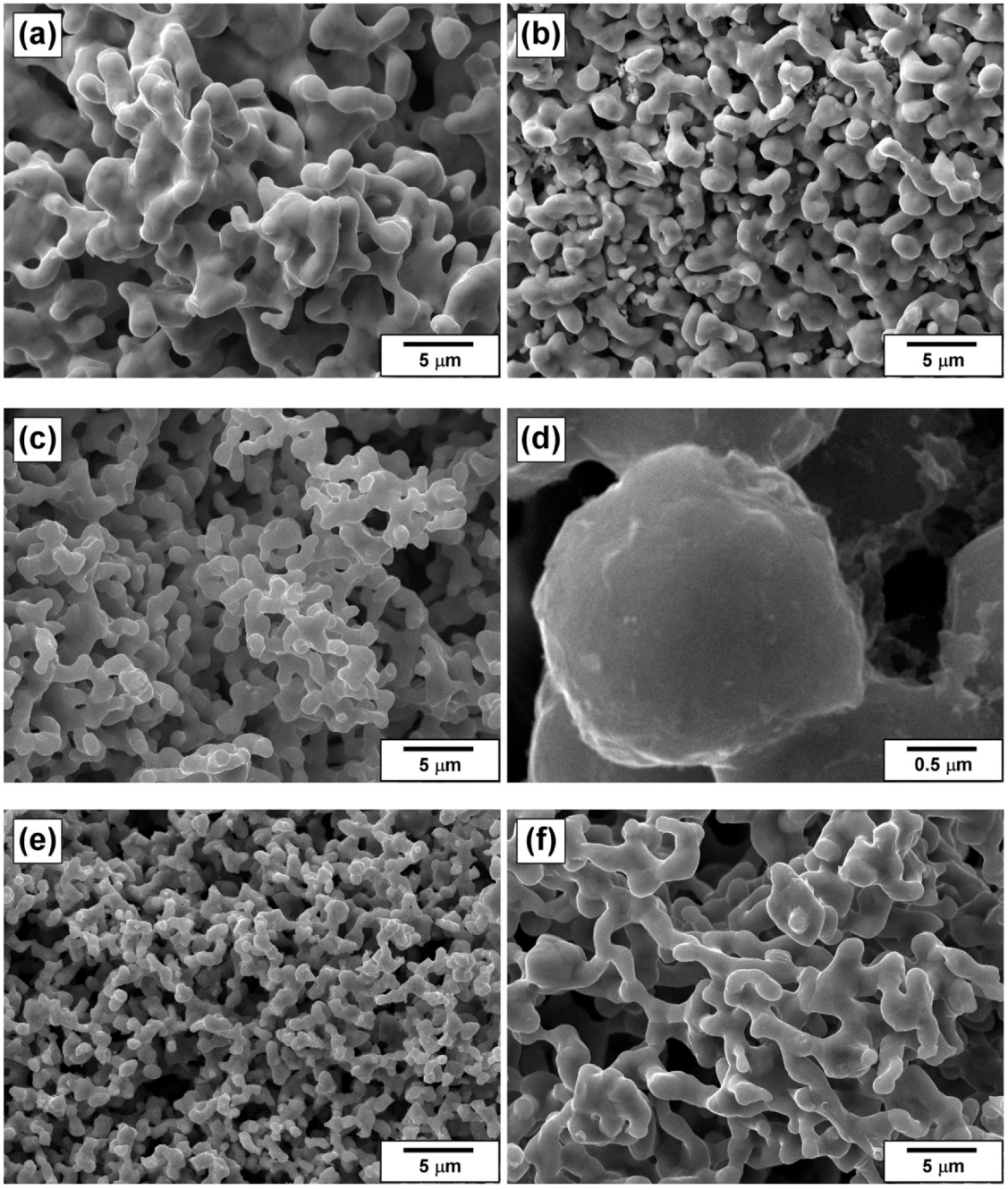

Fig. 2. SEM images of the prepared alloys: a – Ni(92)Mo(8); b – Ni(92)Mo(7)W(1); c, d – Ni(92)Mo(4)W(4); e – Ni(92)Mo(1)W(7); and f – Ni(92)W(8).

Fig. 5 presents the kinetic curves for the CCVD process of DCE over the studied alloys at 600 °C. All the samples exhibit the presence of an induction period (IP) when the weight of the specimen is not changed. After the IP stage, the process proceeds to the second stage of the intensive accumulation of the carbonaceous product (Fig. 5a). The kinetic curves for this stage are characterized by a practically linear function for all the samples. This allows one to calculate a specific rate of carbon deposition (SRCD). The obtained values are summarized in Table 2. As seen, the lowest value of the CNF growth rate (22.4 wt%/min) corresponds to the reference sample Ni(100). The highest SRCD values (43.6–43.8 wt%/min) were demonstrated by three samples: Ni(96)Mo(2)W(2), Ni(94)Mo(3)W(3), and Ni(92)Mo(4)W(4). At the same time, the values of the carbon yield after 2 h of CCVD for these samples are slightly different due to the different duration of the IP stage.

An analysis of the results presented in Table 2 and Fig. 5b allows us to conclude that an introduction of any concentration of molybdenum and tungsten in the composition of the catalyst facilitates the shortening of the IP duration on 3–10 min. Thus, the addition of 4 wt% W and 4 wt% Mo shortens the IP on 3 and 7 min, respectively. The

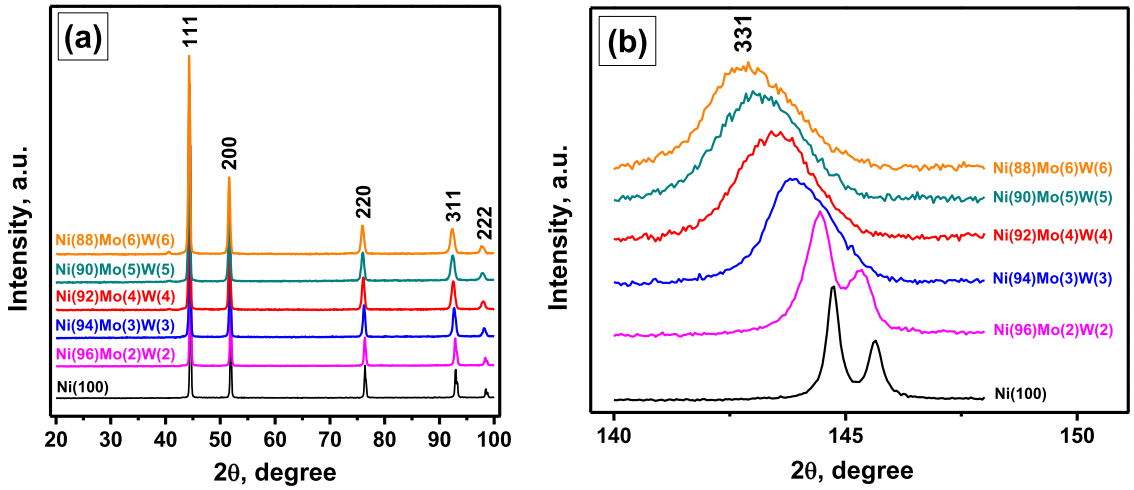

Fig. 3. XRD patterns for the synthesized Ni-Mo-W samples in a 2θ region of 20–100° (a) and in a far-angle region of 140–150° (b).

Table 1
Lattice parameters of Ni-Mo, Ni-Mo-W, and Ni-W alloys.

Total content of alloying metal (x), %	Lattice parameters of the alloy		
	Ni (100-x)Mo (x)	Ni (100-x)W (x)	Ni (100-x)Mo (x/2)W (x/2)
0	3.523		
2	–	3.526	3.526
4	3.534	3.529	3.531
6	3.538	3.532	3.534
8	3.542	3.535	3.539
10	3.548	–	3.542
12	–	3.538	3.544

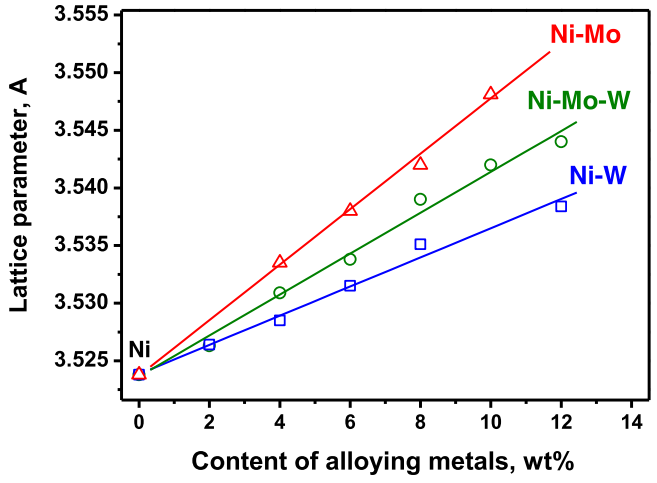

Fig. 4. Dependence of the lattice parameter on the content of alloying metals in Ni-Mo, Ni-W, and Ni-Mo-W alloys.

shortest IP of 11 min was observed in the case of Ni(92)Mo(4)W(4) sample (Table 2).

Besides the IP duration, Table 2 also presents the experimental data on SRCD, carbon yield after 2 h of the CCVD process, and values of the bulk density. Taking into consideration all the presented results, it can be summarized that the highest catalytic activity in CCVD of DCE is demonstrated by triple alloys containing Mo and W in a concentration range from 2 to 4 wt% of each metal. All these samples are characterized by quite similar rates of carbon deposition but differ in the duration of IP. The average value of the carbon yield for the most active sample after 2 h of the reaction was found to exceed 48.2 g_{CNF}/g_{cat}, which is 1.5–2 times higher than the productivity of pure nickel and reference bimetallic Ni-Mo and Ni-W catalysts. Thereby, the joint introduction of W and Mo into Ni lattice in a total concentration of 4–8 wt% facilitates the appearance of a synergetic effect consisted of a sharp increase of the catalytic activity of ternary Ni-Mo-W alloys.

According to the SEM images shown in Fig. 6, the carbon product formed as a result of the CCVD process is represented by the totality of segmented carbon nanofibers with a high degree of defectiveness of fibers' structure and packing. Due to such a disordered structure, the specific surface area, measured by the low-temperature nitrogen adsorption, can exceed 300 m^2/g. The catalytic particles of the alloys are incorporated into the structure of the fibers and can catalyze the simultaneous formation of 2–4 fibers in different directions (Fig. 6a, d, f). The segmented structure of the fibers is well seen in the presented images. Such a secondary structure is typical for the carbon nanofibers resulting from the decomposition of chlorine-substituted hydrocarbons over nickel alloys [36,37]. The average diameter of CNF lies in a range of 0.3–1 μm, which is comparable with the domain size of the initial alloys (see Fig. 2c, d).

The structure of the carbon product obtained over the triple Ni-Mo-W alloys via the CCVD of DCE resembles that for the sample grown over the binary Ni-W system. The disintegration of the Ni-Mo-W alloys as a result of their interaction with the aggressive reaction mixture leads to the formation of dispersed particles functioning as sites of the carbon nanofibers growth. These metal particles are well seen in the SEM images as bright light spots. The morphology of the formed CNF can be divided into two categories: submicron fibers of a segmented structure and thin carbon fibers of about 50 nm in diameter (Fig. 6c). It is assumed that the formation of thin fibers occurs due to the second stage of carbon erosion. The primary metal particles of submicron size catalyzing the growth of thick segmented structures undergo the metal dusting process [44]. The secondary structure of the segmented fibers reflects a discrete character of the graphite-like phase deposition, which is defined by the participation of chlorine in the chemical transformations over the surface of metal particles [34].

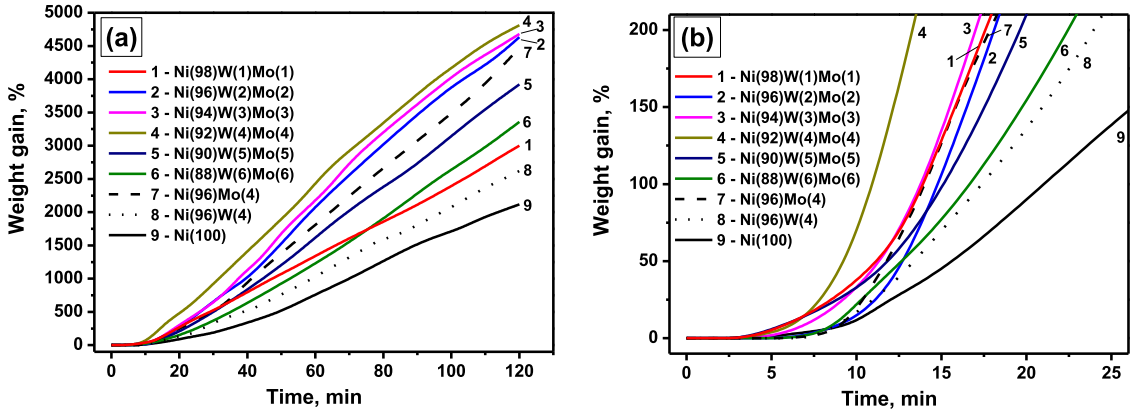

Fig. 5. Kinetics of the CCVD of 1,2-dichloroethane over triple Ni-Mo-W alloys and reference samples at 600 °C: a – the 2-h curves; b – starting area of the curves.

The carbon samples were characterized by low-temperature nitrogen adsorption. The isotherm for Ni(96)Mo(4) sample, as an example, is shown in Fig. 7. Note that the adsorption isotherms for all the other samples are quantitatively similar and have the same shape, which corresponds to Type II, according to the IUPAC classification [45]. As seen from Fig. 7, there is no significant micropore step under the low pressures. An infinite increase of adsorption occurs at P/P° aspiring 1.0. The hysteresis loop is very narrow (see the right-bottom inset in Fig. 7) and can be attributed to type H3. Type H3 character with small but noticeable cavitation step around P/P° ca 0.45 does not allow considering the desorption branch as equilibrium. Thus, all further considerations are made for the adsorption branch. The isotherms of the observed kind are typical to snarly-packed carbon filaments and characterize the samples as meso- and macroporous. The specific surface area values calculated by means of MA-BET technique [46] along with the equivalent amount of liquid nitrogen adsorbed under P/P° = 0.98, which can be attributed to the pore volume if there would be no macroporosity, are presented in Table 3. Additionally, we considered the t-graphs [47] of the isotherms applying the reference t-curve for the Cabot BP 280 non-graphitized carbon black, which was used to parameterize the modern DFT-based methods of characterization of porous carbons [48]. The typical t-graph (sample Ni(96)Mo(4)) is shown in a left-top inset in Fig. 7. One can consider two linear-like regions on the t-graph. The linear regression of the left region gives the line that comes through the origin, indicating the absence of a considerable amount of micropores. The corresponding slopes recalculated to the specific surface area values ($A_{1st\ layer}$, Table 3) are surprisingly close to the BET surface area values. The regression line of the right region on the t-graph corresponds to the polymolecular adsorption. In this case, the intercept is positive. At the same time, in our opinion, it cannot be attributed to the micropores' action due to the absence of adsorption points above the regression lines characteristic to micropores [49], and accounting relatively low values of C_{BET}. The slope of the right region regression line can be attributed to the surface area accessible after the first adsorption layer formation since adsorption is very similar to the macroporous reference. The observed difference between the A_{BET} and $A_{1st\ layer}$ values, from one hand, and the A_t values, from another one, allow assuming the considerable molecular roughness of the investigated samples surface. This roughness does not affect the formation of the adsorption layers above the first layer, as shown in the inset in Fig. 7.

Fig. 8 demonstrates the Raman spectra in a band area of the first and second orders for the CNF formed on the Ni(96)Mo(2)W(2) and Ni(88)Mo(6)W(6) samples. These spectra are typical for all the samples of the studied series. For the samples under consideration, the combination scattering spectra of the first order are represented by the G band at ~1595 cm^{-1}, corresponding to the allowed vibrations E_{2g} of a hexagonal lattice of graphite [50], and the disorder-induced D band of activated A_{1g} mode due to the finite crystal size [51,52] at ~1345 cm^{-1}. The band D_2 at ~1618 cm^{-1} is attributed to a disordered graphitic lattice (surface graphene layers, E_{2g}-symmetry) [53]. The bands D_3 at ~1500 cm^{-1} and D_4 at ~1200 cm^{-1} assigned to an amorphous carbon and a disordered graphitic lattice (A_{1g}-symmetry) or polyenes [54] are typical for soot and related carbonaceous materials. Their relative intensities $I_{D3/G}$ and $I_{D4/G}$ are ~0.21 and ~0.15, respectively. The second-

Table 2
Experimental data for the CCVD of 1,2-dichloroethane over triple Ni-Mo-W alloys and reference samples at 600 °C for 2 h.

#	Sample	P100*, min	SRCD**, wt%/min	Carbon yield, g/g (alloy)	Bulk density of CNM, g/ml
1	Ni(98)Mo(1)W(1)	14.0	30.5	30.2	0.046
2	Ni(96)Mo(2)W(2)	14.8	43.8	46.3	0.136
3	Ni(94)Mo(3)W(3)	14.5	43.7	46.8	0.176
4	Ni(92)Mo(4)W(4)	11.0	43.6	48.2	0.154
5	Ni(90)Mo(5)W(5)	15.2	37.2	39.2	0.124
6	Ni(88)Mo(6)W(6)	16.6	31.9	33.6	0.100
7	Ni(100)	21.0	22.4	21.2	0.031
8	Ni(96)W(4)	17.9	25.4	26.1	0.069
9	Ni(96)Mo(4)	13.9	41.4	33.7	0.107

* P100 is a period required to reach 100% weight gain.
** SRCD is a specific rate of carbon deposition.

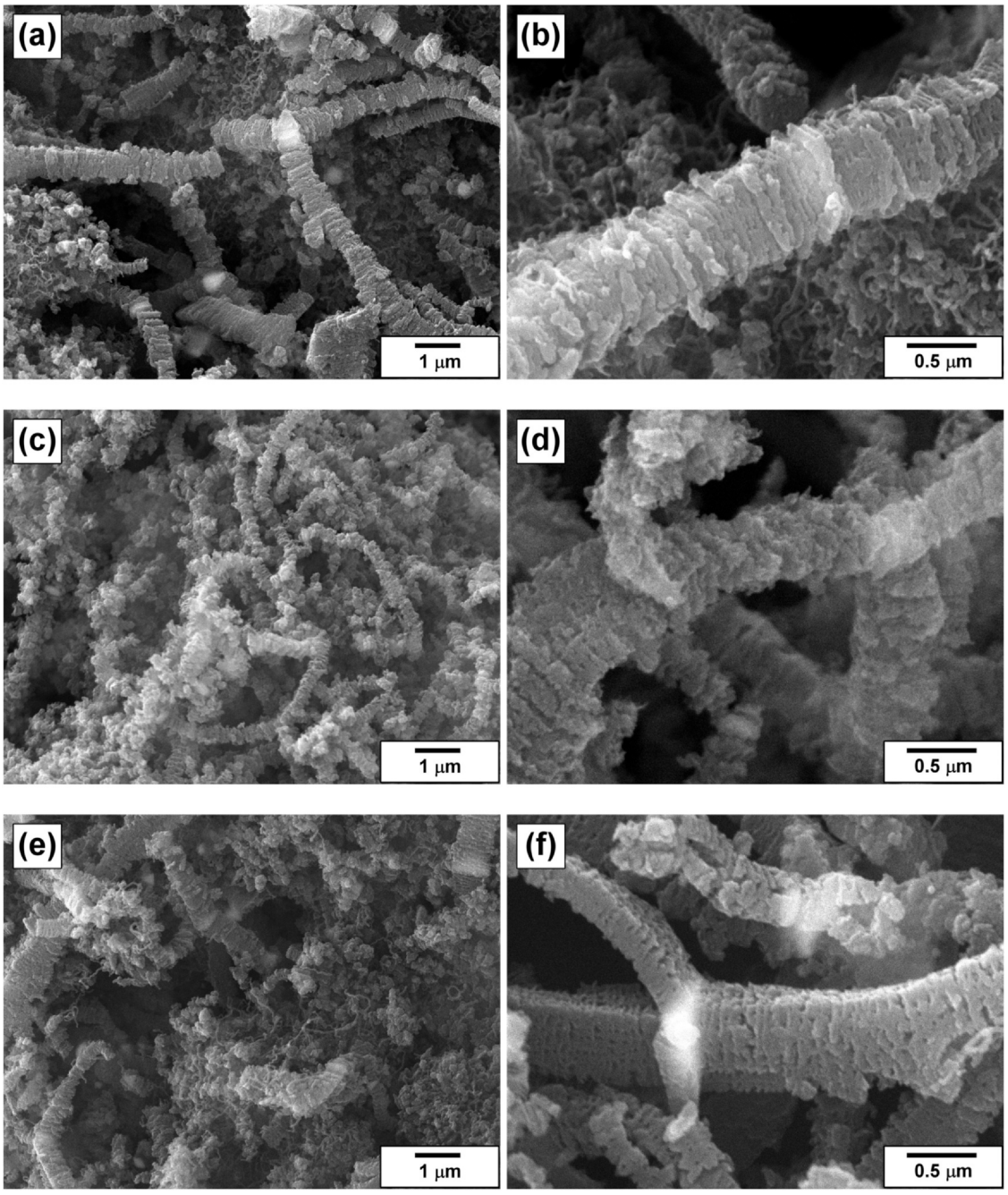

Fig. 6. SEM images of the carbon nanofibers grown over the alloyed catalysts: a, b – Ni(96)W(4); c, d – Ni(96)Mo(4); e, f – Ni(92)Mo(4)W(4).

order bands (2D, D + D_2, and $2D_2$) are well-marked and have a half-width HWNM of ~120 cm^{-1}. A standard set of the 2D, D + D_2, $2D_2$, and G^* ~ D_4 + D bands is enough for the second-order bands' curve fitting.

As follows from Fig. 9a, a L_a in-plane cluster diameter, calculated as $I_D/I_G = C'(\lambda)\cdot L_a^2$, according to Ferrari and Robertson [52], diminishes with a decrease in the Ni content in the samples from 96% to 88%. A characteristic average value of L_a was found to be 17.7 Å. Along with this, the HWHM G values changed from 44 to 50 cm^{-1}, which corresponds to a transition area between two types of approximation curves. The average values of the L_a in-plane cluster diameter obtained using $I_D/I_G = C(\lambda)\cdot L_a$, according to Tuinstra and Koenig [51], can be as high as 25.5 Å. A decrease in the Ni content more significantly increases the relative intensities of the D_3/G and D_4/G bands (Fig. 9b), which are characteristic for soot and related amorphous materials.

The XRD patterns in a 2θ range of 20–60° for the initial Ni(92)Mo(4)W(4) alloy and carbon products obtained after 1 and 2 h of CCVD process are compared in Fig. 10. In the case of initial alloy, the intense reflexes 111 and 200 only are observed. These reflexes correspond to the face-centered cubic (fcc) structure of the alloy. For the

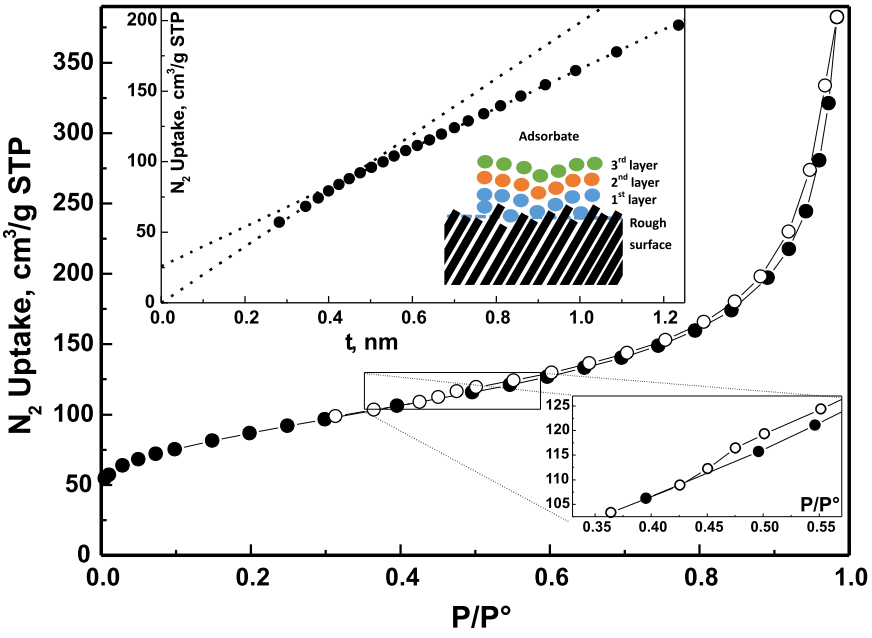

Fig. 7. Nitrogen adsorption isotherm (77.4 K) for the carbon nanofibers grown on the Ni(96)Mo(4) sample. The top inset presents the isotherm in t-graph coordinates and the scheme explaining the difference between the first adsorbed layer capacity and the capacities of the upper layers due to the surface sub-nanometer roughness. The bottom-right inset enlarges the cavitation step on the desorption branch.

Table 3
Textural characteristics according to the nitrogen porosimetry at 77.4 K.

#	Sample	A_{BET}, m^2/g	C_{BET}	$A_{1st\ layer}$, m^2/g	A_t, m^2/g	Right regression line intercepts on *t*-graphs, $li_{q.N2}$, cm^3/g	$V_{liq.N2\ at\ p/p°=0,98}$, cm^3/g
1	Ni(96)Mo(2)W(2)	310	205	309	222	0.039	0.57
2	Ni(94)Mo(3)W(3)	303	212	302	207	0.042	0.53
3	Ni(92)Mo(4)W(4)	298	216	297	202	0.043	0.51
4	Ni(90)Mo(5)W(5)	301	203	299	223	0.036	0.51
5	Ni(88)Mo(6)W(6)	260	228	259	188	0.029	0.51
6	Ni(96)W(4)	307	194	304	207	0.044	0.54
7	Ni(96)Mo(4)	311	177	307	218	0.039	0.56

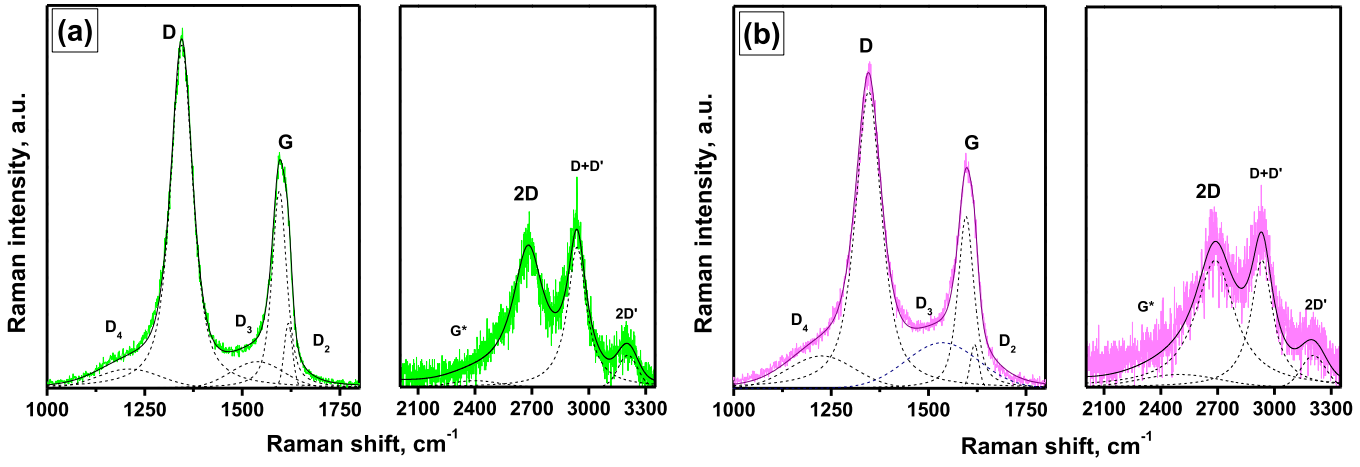

Fig. 8. Raman spectra in a band area of the first and second orders for the carbon nanofibers grown on the alloy catalysts: a – Ni(96)Mo(2)W(2); b – Ni(88)Mo(6)W(6).

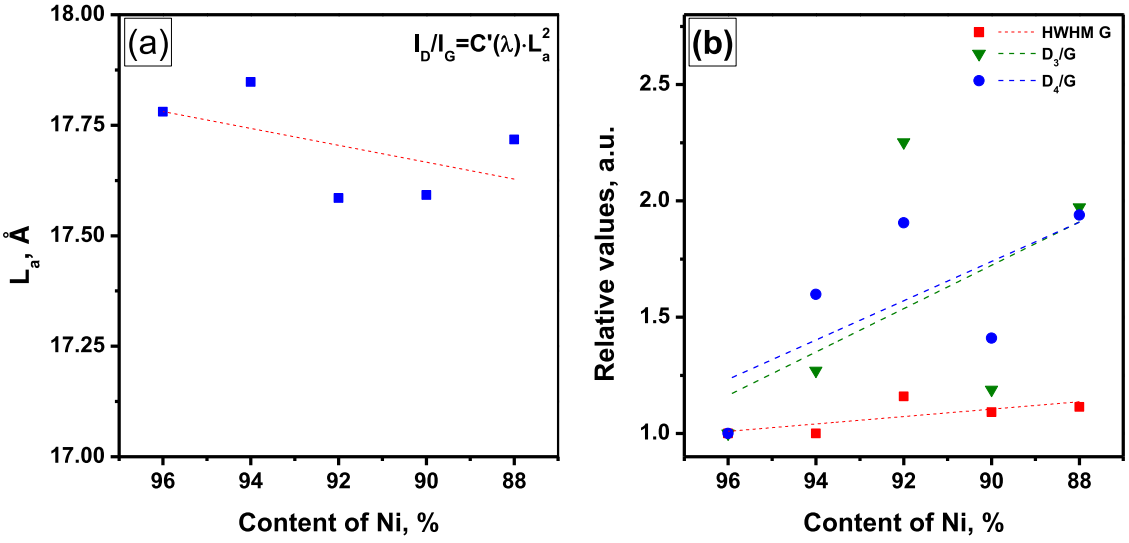

Fig. 9. Dependences of the L_a in-plane cluster diameter (a) and relative values of HWHM G, D_3/G, and D_4/G (b) on the Ni content in the catalysts. The HWHM G, D_3/G, and D_4/G values for the sample Ni(96)Mo(2)W(2) were taken as reference ones.

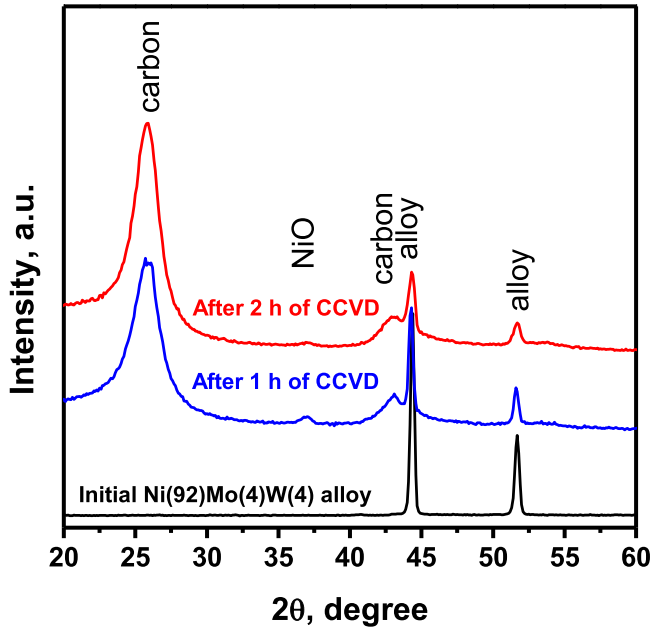

Fig. 10. XRD patterns for the Ni(92)Mo(4)W(4) catalyst and the carbon products resulted from the CCVD process of DCE over this catalyst at 600 °C for 1 and 2 h.

samples after the CCVD process, broad reflexes 002 at 25.8° and 100 at 43.1° of the graphite-like carbon phase have appeared. An increase in the CCVD process duration regularly leads to the enlarged relative intensity of the carbon phase reflexes with regard to the alloy reflexes. It should be noted that deep interaction of the dispersed particles of the alloy with atmospheric oxygen results in the formation of NiO phase and appearance of the corresponding reflex.

The selected TEM micrographs of the CNF samples produced on the studied Ni-based catalysts are shown in Figs. 11 and 12. As seen from Fig. 11, the secondary structure of the carbon nanofibers produced on the reference sample Ni(100) is composed of rather well-expressed segments. Such a kind of carbon fibers was named 'segmented' filaments [26,33]. The segmental structure is characterized by the periodic fluctuations in the density of the graphite-like phase. The submicron-sized Ni crystal in Fig. 11b is seen to be capable of catalyzing the simultaneous growth of four separate carbon filaments. The same can be said about the Ni-Mo particle presented in Fig. 11c. The addition of Mo or W was found to have no noticeable effect on the segmental character of produced CNF.

The TEM images shown in Fig. 12 make it possible to compare the structural features of the carbon products deposited on a series of the triple Ni-W-Mo catalysts with varied content of introduced Mo and W. As seen, the simultaneous presence of Mo and W in the composition of the alloy does not affect the morphology of the produced CNF significantly. The secondary structure of the fibers remains preserved. They are composed of quite regular alternating segments of graphite 'scales' of different density (Fig. 12b, f). Interestingly, the fluctuations in the graphite density can be discerned in two different directions, which are perpendicular to each other (Fig. 12f). At the same time, all the observed active particles were found to be connected with two carbon filaments growing in opposite directions (Fig. 12a, d, e). The carbon filaments are characterized by the submicron size, which is mostly determined by the diameter of the metal crystals that appeared due to the disintegration of the initial triple alloy. In rare cases, the diameter of the carbon filament was close to 0.5–1 μm (Fig. 12c).

In the case of the alloys with the highest content of Mo and W (sample Ni(88)Mo(6)W(6)), the individual metallic particles were found to be surrounded by a graphitic shell of about 50 nm in thickness (Fig. 12e). The formation of such a graphitic shell is associated with either possible deactivation of the CNF growth sites or with the escape of the amorphous carbon from the oversaturated solution of carbon in the Ni(88)Mo(6)W(6) alloy after its cooling to room temperature. The probable interpretation of this fact can be related to an increase in Ni capacity towards carbon, which is resulted from the addition of 12 wt% Mo and W in total [55,56].

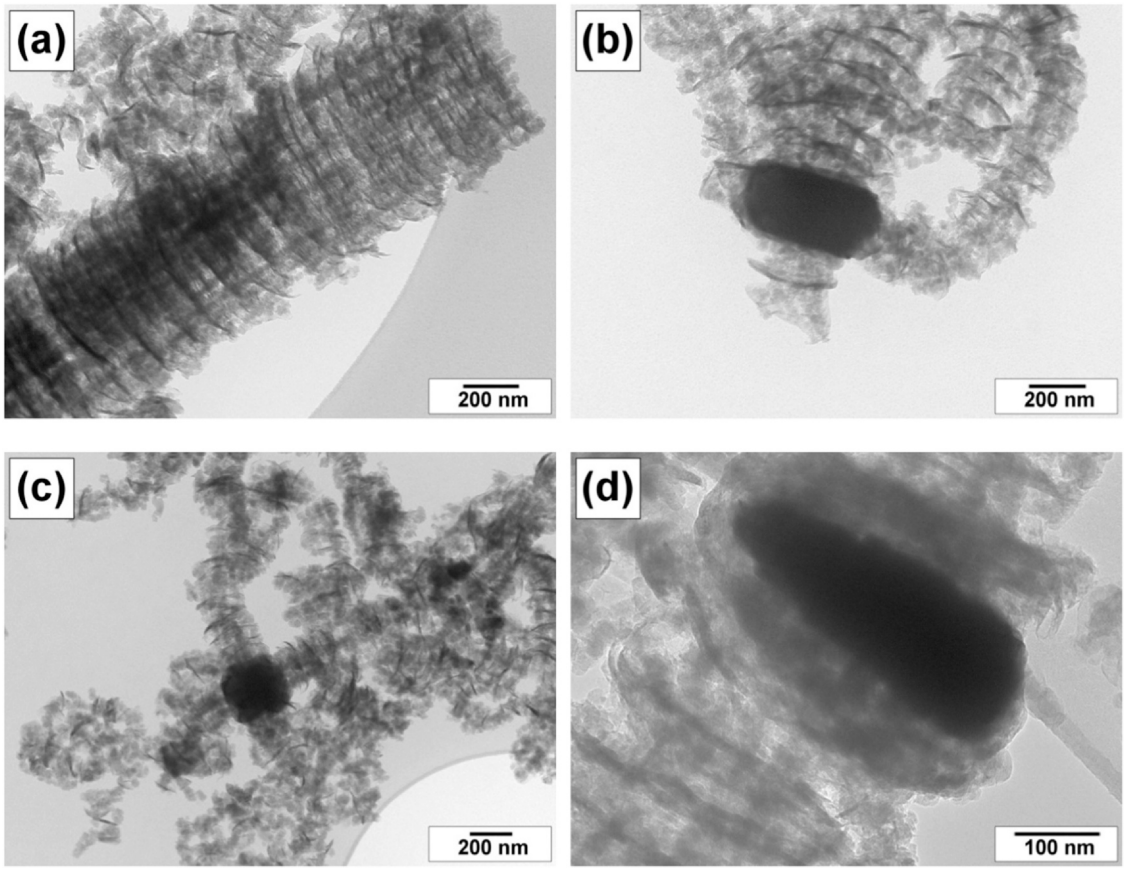

Fig. 11. TEM images of the CNF samples produced on the reference catalysts: a,b – Ni(100); c – Ni(96)Mo(4); d – Ni(96)W(4) via CCVD of DCE at 600 °C for 2 h.

Both scanning and transmission microscopies revealed that the produced carbon nanomaterial is predominantly represented by the assembly of carbon nanofibers. The process of the CNF growth is carried out by the dispersed metallic particles playing the role of the catalytic growth sites. The formation of carbon nanofibers occurs in accordance with the carbide cycle mechanism established by Buyanov [31,57] and comprises several successive stages. The first stage is related to the adsorption and catalytic decomposition of the carbon-containing precursor at the most active faces of the metal crystal. Carbon atoms transfer into the metallic particle, resulting in the formation of the metastable nickel carbide Ni_3C phase. Subsequent decomposition of the nickel carbide phase at the second stage causes the diffusion flux of carbon atoms towards the crystal's faces. These faces are the most complementary to the graphite hexagons. During the third stage, the nucleation of the graphite-like phase and the continuous growth of carbon filaments take place.

4. Conclusions

A facile method for the synthesis of the triple Ni-Mo-W alloys has been developed. The proposed method allows obtaining the single-phase alloys possessing a sponge-like porous structure, which is thought to facilitate greatly the process of their self-disintegration resulting in the spontaneous formation of the catalytically active particles. The simultaneous presence of Mo and W in the composition of the Ni-based alloys was shown to have a synergetic effect in terms of catalytic activity in the CCVD process of 1,2-dichloroethane, used as a representative of the hazardous chlorine-containing organic compound. The carbon nanofibers resulting from this process possess the morphology and secondary structure similar to the carbon deposits observed in the case of reference Ni, Ni-Mo, and Ni-W catalysts. Along with this, the yield of carbon was noticeably higher for the triple Ni-Mo-W alloys. Therefore, the long-term performance and high efficiency of the triple Ni-based alloys with a sponge-like porous structure are reported for the first time.

Funding

This research was funded by the Russian Science Foundation, grant number 16-13-10192.

CRediT authorship contribution statement

Yury V. Shubin: Funding acquisition, Investigation, Formal analysis, Data curation. **Yury I. Bauman:** Methodology, Investigation, Formal analysis. **Pavel E. Plyusnin:** Methodology, Investigation, Formal analysis. **Ilya V. Mishakov:** Resources, Data Curation. **Maria S. Tarasenko:** Methodology, Investigation. **Maxim S. Mel'gunov:** Methodology, Investigation, Formal analysis. **Vladimir O. Stoyanovskii:** Methodology, Investigation, Formal analysis. **Aleksey A. Vedyagin:** Conceptualization, Formal analysis, Data curation, Writing - original draft, Writing - review & editing.

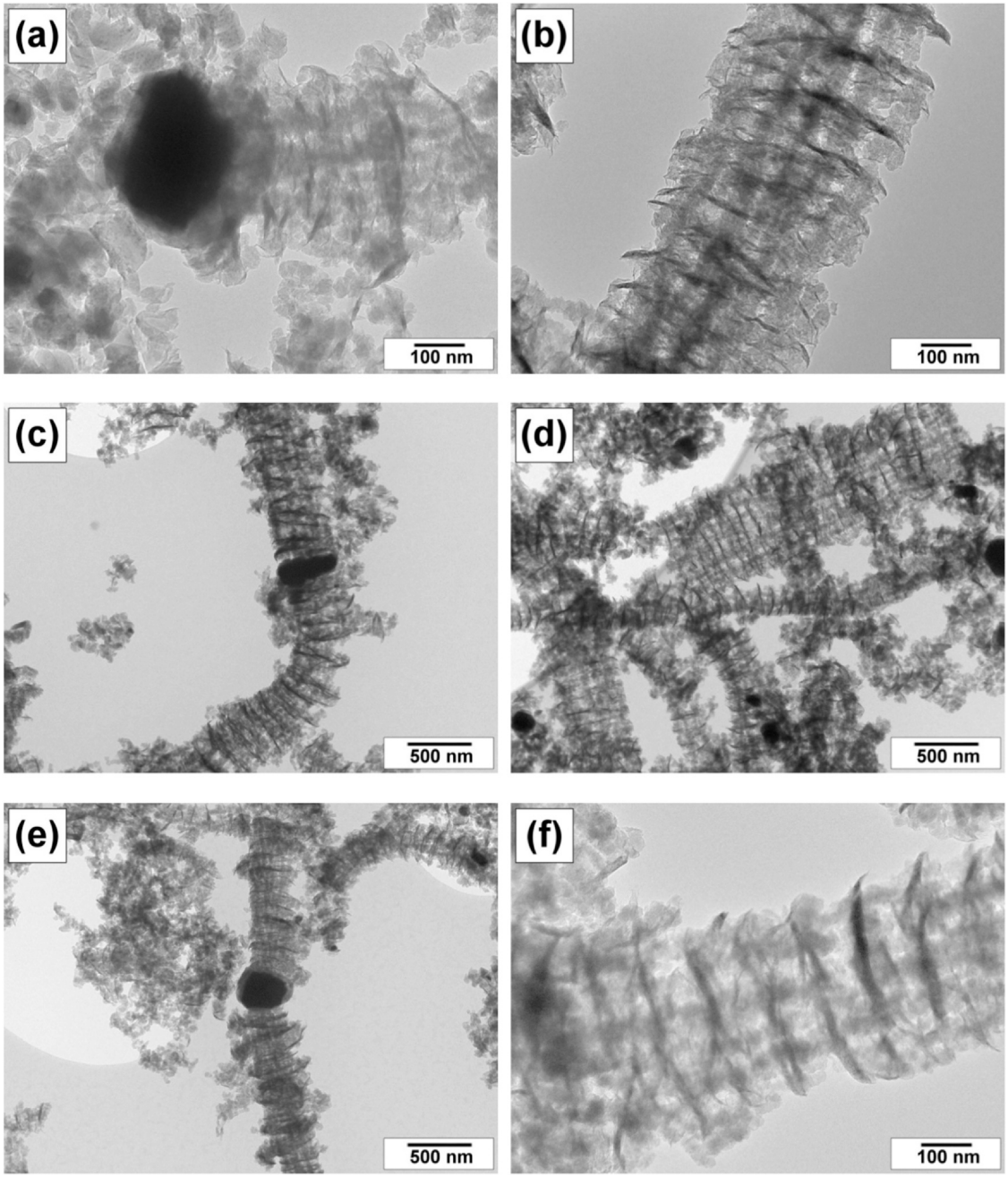

Fig. 12. TEM images of the CNF samples produced on the triple Ni-W-Mo alloys: a,b – Ni(96)Mo(2)W(2); c,d – Ni(92)Mo(4)W(4); e,f – Ni(88)Mo(6)W(6) via CCVD of DCE at 600 °C for 2 h.

Declaration of Competing Interest

The authors declare that they have no known competing financial interests or personal relationships that could have appeared to influence the work reported in this paper.

Acknowledgment

Characterization of the samples was performed using the equipment of the Center of Collective Use' National Center of Catalysts Research' and Krasnoyarsk Regional Center of Research Equipment of Federal Research Center' Krasnoyarsk Science Center SB RAS'.

References

[1] J. Falandysz, A. Fernandes, E. Gregoraszczuk, M. Rose, The toxicological effects of halogenated naphthalenes: a review of aryl hydrocarbon receptor-mediated (dioxin-like) relative potency factors, J. Environ. Sci. Health C Environ. Carcinog. Ecotoxicol. Rev. 32 (2014) 239–272.

[2] R. Jayaraj, P. Megha, P. Sreedev, Organochlorine pesticides, their toxic effects on living organisms and their fate in the environment, Interdiscip. Toxicol. 9 (2016) 90–100.

[3] T.Q. Doan, H.F. Berntsen, S. Verhaegen, E. Ropstad, L. Connolly, A. Igout, M. Muller, M.L. Scippo, A mixture of persistent organic pollutants relevant for human exposure inhibits the transactivation activity of the aryl hydrocarbon receptor in vitro, Environ. Pollut. 254 (2019) 113098.

[4] L. Fabelova, C.A. Loffredo, J. Klanova, K. Hilscherova, M. Horvat, J. Tihanyi, D. Richterova, L. Palkovicova Murinova, S. Wimmerova, R. Sisto, A. Moleti, T. Trnovec, Environmental ototoxicants, a potential new class of chemical stressors, Environ. Res. 171 (2019) 378–394.

[5] M.J. LeBaron, J.A. Hotchkiss, F. Zhang, M.W. Koehler, D.R. Boverhof, Investigation of potential early key events and mode of action for 1,2-dichloroethane-induced mammary tumors in female rats, J. Appl. Toxicol. (2020) jat.4048, https://doi.org/10.1002/jat.4048

[6] L.M. Freitas dos Santos, A.G. Livingston, Extraction and biodegradation of a toxic volatile organic compound (1,2-dichloroethane) from waste-water in a membrane bioreactor, Appl. Microbiol. Biotechnol. 42 (1994) 421–431.

[7] M. Koutinas, I.I.R. Baptista, L.G. Peeva, R.M. Ferreira Jorge, A.G. Livingston, The use of an oil absorber as a strategy to overcome starvation periods in degrading 1,2-dichloroethane in waste gas, Biotechnol. Bioeng. 96 (2007) 673–686.

[8] Y. Shi, X. Du, H. Li, Z. Xu, Q. Wang, X. Meng, F. Li, Effects of soil temperature and agitation on the removal of 1,2-dichloroethane from contaminated soil, Sci. Total. Environ. 423 (2012) 185–189.

[9] S.Y. Wang, S.C. Chen, Y.C. Lin, Y.C. Kuo, J.Y. Chen, C.M. Kao, Acidification and sulfide formation control during reductive dechlorination of 1,2-dichloroethane in groundwater: effectiveness and mechanistic study, Chemosphere 160 (2016) 216–229.

[10] I.A. Al-Baldawi, Removal of 1,2-dichloroethane from real industrial wastewater using a sub-surface batch system with Typha angustifolia L, Ecotoxicol. Environ. Saf. 147 (2018) 260–265.

[11] T.K. Tseng, L. Wang, C.T. Ho, H. Chu, The destruction of dichloroethane over a gamma-alumina supported manganese oxide catalyst, J. Hazard. Mater. 178 (2010) 1035–1040.

[12] X. Ning, D. Deng, H. Fu, X. Qu, Z. Xu, S. Zheng, Ni-PC@SBA-15 derived from nano-sized Ni-MOF-74 confined in SBA-15 as a highly active catalyst for gas phase catalytic hydrodechlorination of 1,2-dichloroethane, Chem. Commun. 56 (2020) 6985–6988.

[13] D.I. Kim, D.T. Allen, Catalytic hydroprocessing of chlorinated olefins, Ind. Eng. Chem. Res. 36 (1997) 3019–3026.

[14] R.J. Meyer, D.I. Kim, D.T. Allen, J.H. Jo, Catalytic hydrodechlorination of 1,3-dichloropropene, Chem. Eng. Sci. 54 (1999) 3627–3634.

[15] C. Sotowa, Y. Watanabe, S. Yatsunami, Y. Korai, I. Mochida, Catalytic dehydrochlorination of 1,2-dichloroethane into vinyl chloride over polyacrylonitrile-based active carbon fiber, Appl. Catal. A Gen. 180 (1999) 317–323.

[16] Q. Huang, X. Xue, R. Zhou, Decomposition of 1,2-dichloroethane over CeO2 modified USY zeolite catalysts: effect of acidity and redox property on the catalytic behavior, J. Hazard. Mater. 183 (2010) 694–700.

[17] M.R. Flid, L.M. Kartashov, Y.A. Treger, Theoretical and applied aspects of hydrodechlorination processes—catalysts and technologies, Catalysts 10 (2020) 216.

[18] H. Rotter, M.V. Landau, M. Herskowitz, Combustion of chlorinated VOC on nanostructured chromia aerogel as catalyst and catalyst support, Environ. Sci. Technol. 39 (2005) 6845–6850.

[19] E.A. Paukshtis, L.G. Simonova, A.N. Zagoruiko, B.S. Balzhinimaev, Oxidative destruction of chlorinated hydrocarbons on Pt-containing fiber-glass catalysts, Chemosphere 79 (2010) 199–204.

[20] M. Mohsenzadeh, S.A. Mirbagheri, S. Sabbaghi, Degradation of 1,2-dichloroethane by photocatalysis using immobilized PAni-TiO2 nano-photocatalyst, Environ. Sci. Pollut. Res. Int. 26 (2019) 31328–31343.

[21] I.I. Kamińska, A. Śrębowata, Active carbon-supported nickel–palladium catalysts for hydrodechlorination of 1,2-dichloroethane and 1,1,2-trichloroethene, Res. Chem. Intermed. 41 (2015) 9267–9280.

[22] E.V. Golubina, T.N. Rostovshchikova, E.S. Lokteva, K.I. Maslakov, S.A. Nikolaev, T.B. Egorova, S.A. Gurevich, V.M. Kozhevin, D.A. Yavsin, A.Y. Yermakov, Chlorobenzene hydrodechlorination on bimetallic catalysts prepared by laser electrodispersion of NiPd alloy, Pure Appl. Chem. 90 (2018) 1685–1701.

[23] Y. Han, C. Liu, J. Horita, W. Yan, Trichloroethene (TCE) hydrodechlorination by Ni Fe nanoparticles: influence of aqueous anions on catalytic pathways, Chemosphere 205 (2018) 404–413.

[24] L. Liu, X. Sun, W. Li, Y. An, H. Li, Electrochemical hydrodechlorination of perchloroethylene in groundwater on a Ni-doped graphene composite cathode driven by a microbial fuel cell, RSC Adv. 8 (2018) 36142–36149.

[25] S. Liu, M. Martin-Martinez, M.A. Álvarez-Montero, A. Arevalo-Bastante, J.J. Rodriguez, L.M. Gómez-Sainero, Recycling of gas phase residual dichloromethane by hydrodechlorination: regeneration of deactivated Pd/C catalysts, Catalysts 9 (2019) 733.

[26] A. Nieto-Márquez, J.L. Valverde, M.A. Keane, Catalytic growth of structured carbon from chloro-hydrocarbons, Appl. Catal. A Gen. 332 (2007) 237–246.

[27] Y.I. Bauman, I.V. Mishakov, A.A. Vedyagin, S.V. Dmitriev, M.S. Mel'gunov, R.A. Buyanov, Processing of organochlorine waste components on bulk metal catalysts, Catal. Ind. 4 (2012) 261–266.

[28] Y.I. Bauman, A.S. Lysakova, A.V. Rudnev, I.V. Mishakov, Y.V. Shubin, A.A. Vedyagin, R.A. Buyanov, Synthesis of nanostructured carbon fibers from chlorohydrocarbons over Bulk Ni-Cr Alloys, Nanotechnol. Russ. 9 (2014) 380–385.

[29] W.-H. Lin, T.-T. Lee, Y.-Y. Li, Chlorine effect on formation of turbostratic carbon nanofibers by a mixture of 1,2-dichloroethane and ethanol, J. Taiwan Inst. Chem. Eng. 45 (2014) 1883–1891.

[30] W.K. Maboya, N.J. Coville, S.D. Mhlanga, The synthesis of carbon nanomaterials using chlorinated hydrocarbons over a Fe-Co/CaCO3 catalyst, South Afr. J. Chem. 69 (2016).

[31] I.V. Mishakov, R.A. Buyanov, V.I. Zaikovskii, I.A. Strel'tsov, A.A. Vedyagin, Catalytic synthesis of nanosized feathery carbon structures via the carbide cycle mechanism, Kinet. Catal. 49 (2008) 868–872.

[32] Y.I. Bauman, I.V. Mishakov, R.A. Buyanov, A.A. Vedyagin, A.M. Volodin, Catalytic properties of massive iron-subgroup metals in dichloroethane decomposition into carbon products, Kinet. Catal. 52 (2011) 547–554.

[33] I.V. Mishakov, A.A. Vedyagin, Y.I. Bauman, Y.V. Shubin, R.A. Buyanov, Synthesis of carbon nanofibers via catalytic chemical vapor deposition of halogenated hydrocarbons, in: L. Chang-Seop (Ed.), Carbon Nanofibers: Synthesis, Applications and Performance, Nova Science Publishers, 2018, pp. 77–181.

[34] Y.I. Bauman, Y.V. Shorstkaya, I.V. Mishakov, P.E. Plyusnin, Y.V. Shubin, D.V. Korneev, V.O. Stoyanovskii, A.A. Vedyagin, Catalytic conversion of 1,2-dichloroethane over Ni-Pd system into filamentous carbon material, Catal. Today 293–294 (2017) 23–32.

[35] Y.I. Bauman, Y.V. Rudneva, I.V. Mishakov, P.E. Plyusnin, Y.V. Shubin, A.A. Vedyagin, Synthesis of filamentary carbon material on a self-organizing Ni–Pt catalyst in the course of 1,2-dichloroethane decomposition, Kinet. Catal. 59 (2018) 363–371.

[36] Y.I. Bauman, I.V. Mishakov, Y.V. Rudneva, A.A. Popov, D. Rieder, D.V. Korneev, A.N. Serkova, Y.V. Shubin, A.A. Vedyagin, Catalytic synthesis of segmented carbon filaments via decomposition of chlorinated hydrocarbons on Ni-Pt alloys, Catal. Today 348 (2020) 102–110.

[37] Y.I. Bauman, Y.V. Rudneva, I.V. Mishakov, P.E. Plyusnin, Y.V. Shubin, D.V. Korneev, V.O. Stoyanovskii, A.A. Vedyagin, R.A. Buyanov, Effect of Mo on the catalytic activity of Ni-based self-organizing catalysts for processing of dichloroethane into segmented carbon nanomaterials, Heliyon 5 (2019) e02428.

[38] Y. Bauman, L. Kibis, I. Mishakov, Y. Rudneva, V.O. Stoyanovskii, A.A. Vedyagin, Synthesis and functionalization of filamentous carbon material via decomposition of 1,2-dichlorethane over self-organizing Ni-Mo catalyst, Mater. Sci. Forum 950 (2019) 180–184.

[39] G.B. Veselov, T.M. Karnaukhov, Y.I. Bauman, I.V. Mishakov, A.A. Vedyagin, Sol-gel-prepared Ni-Mo-Mg-O system for catalytic transformation of chlorinated organic wastes into nanostructured carbon, Materials 13 (2020) 4404.

[40] I.V. Mishakov, N.V. Kutaev, Y.I. Bauman, Y.V. Shubin, A.P. Koskin, A.N. Serkova, A.A. Vedyagin, Mechanochemical synthesis, structure, and catalytic activity of Ni-Cu, Ni-Fe, and Ni-Mo alloys in the preparation of carbon nanofibers during the decomposition of chlorohydrocarbons, J. Struct. Chem. 61 (2020) 769–779.

[41] A. Huang, Y. He, Y. Zhou, Y. Zhou, Y. Yang, J. Zhang, L. Luo, Q. Mao, D. Hou, J. Yang, A review of recent applications of porous metals and metal oxide in energy storage, sensing and catalysis, J. Mater. Sci. 54 (2018) 949–973.

[42] G. Brauer, Handbuch der Praparativen Anorganischen Chemie: in drei Banden/Bd 2, Ferdinand Enke, Stuttgart, Germany, 1978.

[43] W. Kraus, G. Nolze, POWDER CELL – a program for the representation and manipulation of crystal structures and calculation of the resulting X-ray powder patterns, J. Appl. Crystallogr. 29 (1996) 301–303.

[44] Y.I. Bauman, I.V. Mishakov, A.A. Vedyagin, S. Ramakrishna, Synthesis of bimodal carbon structures via metal dusting of Ni-based alloys, Mater. Lett. 201 (2017) 70–73.

[45] M. Thommes, K. Kaneko, A.V. Neimark, J.P. Olivier, F. Rodriguez-Reinoso, J. Rouquerol, K.S.W. Sing, Physisorption of gases, with special reference to the evaluation of surface area and pore size distribution (IUPAC Technical Report), Pure Appl. Chem. 87 (2015) 1051–1069.

[46] M.S. Mel'gunov, A.B. Ayupov, Direct method for evaluation of BET adsorbed monolayer capacity, Microporous Mesoporous Mater. 243 (2017) 147–153.

[47] J.H. de Boer, B.C. Lippens, B.G. Linsen, J.C.P. Broekhoff, A. van den Heuvel, T.J. Osinga, Thet-curve of multimolecular N2-adsorption, J. Colloid Interf. Sci. 21 (1966) 405–414.

[48] G.Y. Gor, M. Thommes, K.A. Cychosz, A.V. Neimark, Quenched solid density functional theory method for characterization of mesoporous carbons by nitrogen adsorption, Carbon 50 (2012) 1583–1590.

[49] K. Kaneko, Determination of pore size and pore size distribution, J. Membr. Sci. 96 (1994) 59–89.

[50] R.J. Nemanich, S.A. Solin, First- and second-order Raman scattering from finite-size crystals of graphite, Phys. Rev. B 20 (1979) 392–401.

[51] F. Tuinstra, J.L. Koenig, Raman spectrum of graphite, J. Chem. Phys. 53 (1970) 1126–1130.

[52] A.C. Ferrari, J. Robertson, Interpretation of Raman spectra of disordered and amorphous carbon, Phys. Rev. B 61 (2000) 14095–14107.

[53] Y. Wang, D.C. Alsmeyer, R.L. McCreery, Raman spectroscopy of carbon materials: structural basis of observed spectra, Chem. Mater. 2 (1990) 557–563.

[54] A. Sadezky, H. Muckenhuber, H. Grothe, R. Niessner, U. Pöschl, Raman microspectroscopy of soot and related carbonaceous materials: spectral analysis and structural information, Carbon 43 (2005) 1731–1742.

[55] E. Jang, H.-K. Park, J.-H. Choi, C.-S. Lee, Synthesis and characterization of carbon nanofibers grown on Ni and Mo catalysts by chemical vapor deposition, Bull. Korean Chem. Soc. 36 (2015) 1452–1459.

[56] Y. Li, X.B. Zhang, X.Y. Tao, J.M. Xu, W.Z. Huang, J.H. Luo, Z.Q. Luo, T. Li, F. Liu, Y. Bao, H.J. Geise, Mass production of high-quality multi-walled carbon nanotube bundles on a Ni/Mo/MgO catalyst, Carbon 43 (2005) 295–301.

[57] V.V. Chesnokov, R.A. Buyanov, The formation of carbon filaments upon decomposition of hydrocarbons catalysed by iron subgroup metals and their alloys, Russ. Chem. Rev. 69 (2000) 623–638.